


Photon diffusion in space and time in a second-order-nonlinear disordered medium

Rabisankar Samanta,¹ Romain Pierrat^{2,*}, Rémi Carminati^{2,3} and Sushil Mujumdar^{1,†}

¹*Nano-optics and Mesoscopic Optics Laboratory, Tata Institute of Fundamental Research, 1 Homi Bhabha Road, Mumbai 400 005, India*

²*Institut Langevin, ESPCI Paris, PSL University, CNRS, 1 rue Jussieu, 75005 Paris, France*

³*Institut d'Optique Graduate School, Université Paris-Saclay, 91127 Palaiseau, France*

 (Received 18 May 2023; revised 9 October 2023; accepted 11 October 2023; published 2 November 2023)

We report experimental and theoretical investigations of photon diffusion in a second-order-nonlinear disordered medium under conditions of strong nonlinearity. Experimentally, photons at the fundamental wavelength ($\lambda = 1064$ nm) are launched into the structure in the form of a cylindrical pellet, and the second-harmonic ($\lambda = 532$ nm) photons are temporally analyzed in transmission. For comparison, separate experiments are carried out with incident green light at $\lambda = 532$ nm. We observe that the second-harmonic light peaks earlier compared to the incident green photons. Next, the sideways spatial scattering of the fundamental as well as second-harmonic photons is recorded. The spatial diffusion profiles of second-harmonic photons are seen to peak deeper inside the medium in comparison to both the fundamental and incident green photons. In order to give more physical insights into the experimental results, a theoretical model is derived from first principles. It is based on the coupling of transport equations. Solved numerically using a Monte Carlo algorithm and experimentally estimated transport parameters at both wavelengths, it shows excellent semiquantitative agreement with the experiments for both fundamental and second-harmonic light.

DOI: [10.1103/PhysRevA.108.053501](https://doi.org/10.1103/PhysRevA.108.053501)

I. INTRODUCTION

Electromagnetic wave propagation and scattering are ubiquitous in diverse fields such as optics, condensed-matter physics, biology, atmospheric optics, etc. [1]. Among various related phenomena, the diffusion of light has attracted maximum attention in the last few decades [2]. Two factors have primarily motivated these studies, namely, the occurrence of the diffusion of light in tissues [3] and the parallels between light diffusion and electron propagation in disordered conductors [4]. The first subfield, namely, diffusion in tissues, has led to significant signs of progress in imaging inclusions in living media [5], with the aim of replacing hazardous high-energy radiation. The second domain overlaps with condensed-matter studies and is intended to understand mesoscopic effects in light transport in disordered media. Indeed, studies on mesoscopic optics have led to better insights into electronic transport, such as the transition from the diffusion regime to the localization regime [6] upon a sufficient increase in disorder.

A primary reason for the success of these studies in the optical domain has been the inherent noninteracting nature of the photons, as well as the possibility to directly image the intensity distribution, which makes analyses easier than for electrons. Interestingly, photon propagation allows for additional aspects of transport, such as amplification and nonlinearity. On the one hand, coherent amplification accompanied by diffusion or localization has led to the creation

of novel optical sources named random lasers [7–12]. On the other hand, studies coupling nonlinearity with the disorder have attracted growing attention [13–26]. For instance, a great deal of effort has been focused on the effects of $\chi^{(3)}$ nonlinearity on Anderson localization [16–18], wherein the question of whether nonlinearity subjugates localization is still an open question [19]. Experimental attempts to address this problem in one-dimensional systems showed that the localized mode continues to exist under introduced nonlinearity [20]. Theoretically, the effects of $\chi^{(3)}$ nonlinearity on coherent backscattering (or weak localization) have also been documented [21,22]. Likewise, $\chi^{(2)}$ materials, particularly relevant to second-harmonic generation (SHG) [27], have been studied in the regimes of diffusion and weak localization [23–26]. Specifically, several consequences of random quasi phase matching in disordered $\chi^{(2)}$ materials were discussed in recent years [28–30]. Furthermore, speckle dynamics in these materials were recently quantified and theoretically modeled [31,32]. Interestingly, second-harmonic generation in a diffusive material creates a unique paradoxical situation of incoherent transport, i.e., diffusion, coupled with an inherently coherent phenomenon of second-harmonic generation and hence is of fundamental research interest. Over the years, a few theoretical [33,34] and experimental reports [35] have addressed this peculiar scenario. In one of the earliest reports, Kravtsov *et al.* [33] theoretically studied two models of disorder, namely, point scatterers in a nonlinear medium and grainy nonlinear scatterers, and observed sharp peaks in the angular distribution of backward diffuse second-harmonic light. In another approach, Makeev *et al.* theoretically studied the diffusion of second-harmonic (SH) light in a colloidal suspension of spherical nonlinear particles, wherein they found

*romain.pierrat@espci.psl.eu

†mujumdar@tifr.res.in

that the average SH intensity was independent of the linear scattering properties of the medium [34]. In the experimental effort using GaP powders, a consistent picture that described the second-harmonic intensity distribution in the sample was obtained via the diffusion equation, which invoked nonlinearity as a conversion rate [35].

The various models described above successfully invoked the scenario of weak nonlinearity, wherein the nonlinearity did not affect the distribution of fundamental photons. However, these works focused on the spatial behavior of fundamental and second-harmonic light, while no attention was paid to the temporal behavior, under ultrashort-pulse illumination. In this work, we address this question and others in light of experiments and of a theoretical model. We carry out spatial and temporal investigations of light propagating through a strongly disordered potassium dihydrogen phosphate (KDP) pellet. We diagnose pulse propagation through the system and measure the transport mean free paths for the fundamental and second-harmonic light using the transmitted pulses. Subsequently, we measure the longitudinal spatial distribution of both components. To give more physical insights into the processes at play, we build from first principles a theoretical model involving the coupling of two radiative-transfer equations (RTEs). Solved numerically using a Monte Carlo scheme, the model gives reliable results compared to the experiment. In Sec. II, we introduce the samples and the experiments, and we present all experimental results. In Sec. III, we present the theoretical model as well as the associated numerical simulations in the same geometry as in the experiments. The discussion and conclusion are given in Sec. IV.

II. SAMPLES AND EXPERIMENTS

We exploited commercially available KDP (EMSURE ACS) as our nonlinear material. It has a large second-order optical nonlinearity (~ 0.43 pm/V). A fine powder of KDP was realized after 10 min of ball milling. Figure 1(a) depicts the scanning electron micrograph image of KDP grains, while the inset shows the size distribution of the KDP grains, with grain sizes in the range of 2 to 8 μm . The size distribution (red bar graph) is approximately log normal (yellow line), peaking at 3.11 μm . A pellet with length $L = 5$ mm and radius $a = 0.5$ cm was created under a hydraulic press. The pellet was baked to remove remnant moisture at a temperature of 80 $^{\circ}\text{C}$, which was far below the transition temperature (190 $^{\circ}\text{C}$ [36]) of KDP. Before going to the main experiment, we evaluated the effective refractive indices and internal reflection coefficients that will be used later as input parameters in our theoretical model. Using the Maxwell-Garnett formula [37] (see Appendix A regarding the use of the Maxwell-Garnett formula), the real parts of the effective refractive indices of the pellet were found to be $n_r(2\omega) = 1.45$ and $n_r(\omega) = 1.43$ at $\lambda = 532$ nm and $\lambda = 1064$ nm, respectively. The internal power reflection coefficients at $\lambda = 532$ nm and $\lambda = 1064$ nm are estimated to be $R(2\omega) = 0.53$ and $R(\omega) = 0.52$, respectively [38] (see Appendix A for a detailed derivation of the internal reflection coefficient).

A schematic of the experimental setups is depicted in Figs. 1(b) and 1(c). Two different experiments were performed. For the temporal measurements [Fig. 1(b)],

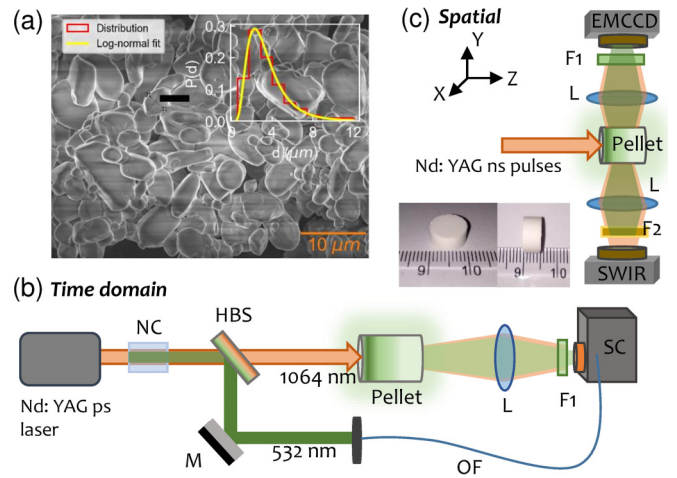


FIG. 1. (a) SEM image of particles. The scale bar is 10 μm . Inset: Distribution of particle size. (b) Schematic for temporal measurements. Abbreviations: NC, nonlinear crystal; HBS, harmonic beam splitter; M, mirror; L, lens; F1, filter (for $\lambda = 532$ nm); OF, optical fiber; SC, streak camera. (c) Schematic of the experiment on spatial diffusion. Abbreviations: L, lens; F1, F2, filters; SWIR, short-wavelength infrared; EMCCD, electron-multiplying charge-coupled device. Insets show a pellet with a 1-cm diameter and a length of 5 mm.

Nd:yttrium aluminum garnet (YAG) picosecond laser pulses (EKSPLA, PL2143B), with pulse width ~ 30 ps at the fundamental wavelength of $\lambda = 1064$ nm (hereafter referred to as IR) and beam waist ~ 5 mm, were made incident on the front face of the pellet. The second-harmonic-generated light (hereafter referred to as SHG) that was transmitted from the back face was directed into the streak camera (Optronics SC-10). The streak camera possesses a temporal resolution of less than 3 ps, and its specified spectral sensitivity ranges from 200 to 950 nm. The spectral range of the streak camera did not allow for measuring the IR pulse. A small part of the second-harmonic light generated by a clear nonlinear crystal was directed toward the marker pulse input of the streak camera to calibrate the zero of the time axis. For the spatial measurements [Fig. 1(c)], the pellet was pumped with the fundamental of the Nd:YAG nanosecond laser (pulse width ~ 5 ns, repetition rate of 10 Hz). The pulsed IR beam was launched normally onto the front face of the pellet. The scattered IR photons were imaged from one side of the pellet by the combination of a lens and an InGaAs CCD, as shown in Fig. 1. Simultaneously, a silicon CCD along with a lens was employed to measure the internally generated and scattered second-harmonic photons (SHG). For comparison for later discussion, in both the temporal and spatial experiments, we also externally launched frequency-doubled green light from the source laser ($\lambda = 532$ nm, hereafter referred to as incident green, or IG), whose temporal transmitted profile and spatial scattering profile were measured separately by the same streak camera and silicon CCD, respectively. The CCD images provided the spatial variation of light intensity along the length of the pellet.

Our sample consists of a large number of KDP microcrystals with random orientations. The incident photons

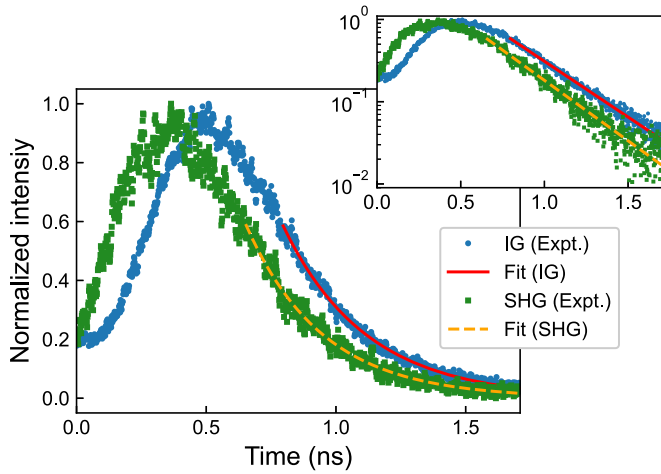


FIG. 2. Experimental temporal diffusion profiles of SHG (green squares) and IG (blue dots) in a pellet with $L = 5$ mm. The SHG signal peaks earlier in time. The orange dashed and red solid lines fit the exponential decays for SHG and IG, respectively. Inset: diffusion profiles on the semilog scale show comparable decay lengths.

experience multiple scattering due to the refractive index mismatch between the microcrystals and the background medium. SHG photons are generated at random positions within the medium by the crossing of two IR photons and also undergo multiple scattering. At large optical thickness and long times, we can expect the transmitted multiply scattered IR and SHG intensities to follow a diffusion process, as confirmed by the spatial intensity profiles shown below.

The experimental temporal profiles of SHG (green squares) and IG (blue dots) in the pellet, plotted in Fig. 2, exhibit a classic diffusive behavior. We observe an interesting trend in the transmission in which SHG photons have shorter residence times than IG photons, given that the SHG profile peaks earlier. The temporal profiles of SHG and IG show clear exponentially decaying tails, as evidenced in the inset on a logarithmic scale. Interestingly, the decay rates for the two curves are also very similar, a fact which we will return to in our theoretical work. The tails were fit by the expression $A \exp(-\Gamma t)$, with Γ being the decay rate. The estimated decay rates fitted to numerous temporal profiles of the same sample amount to 3.17 ± 0.13 and $3.25 \pm 0.11 \text{ ns}^{-1}$ for the SHG and IG, respectively. These values are as close as a fitting routine can provide. The apparent deviation may therefore be due to the strong noise level. The orange dashed and red solid lines in Fig. 2 correspond to the fits for SHG and IG, respectively. Nonetheless, we emphasize here that only the IG data can be fit *a priori* using diffusion theory. Although we use the same analysis for the SHG light, the fact that it follows a similar diffusion equation cannot be justified based on an existing theory. The theory developed in the next section will elaborate on this part and also justify the comparable decays seen in the experiments. In the presence of absorption and side loss, the decay rate Γ in a cylindrical system can be written as [39]

$$\Gamma(2\omega) = \mathcal{D}(2\omega) \left[\frac{\alpha_1^2}{a_e(2\omega)^2} + \frac{\pi^2}{L_e(2\omega)^2} + \frac{3}{\ell_t(2\omega)\ell_a(2\omega)} \right], \quad (1)$$

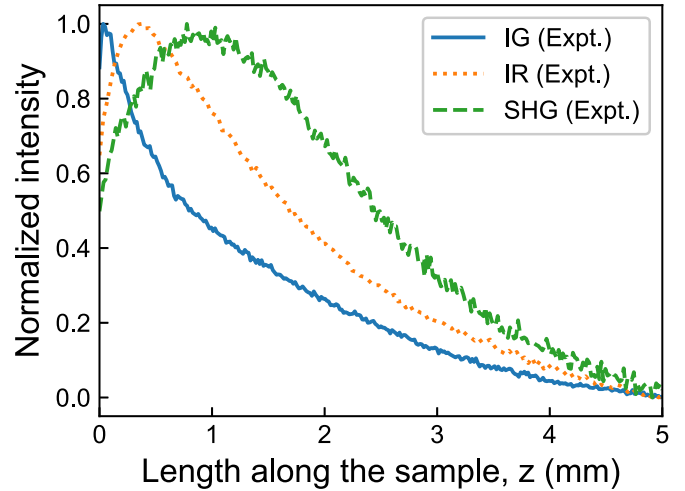


FIG. 3. Experimental spatial intensity profiles of incident green (IG; blue solid line), fundamental infrared (IR; orange dotted line), and second-harmonic-generated green (SHG; green dashed line) light for the $L = 5$ mm pellet. The SHG signal peaks much deeper in the sample, and IG peaks closest to the entry face inside the pellet, followed by IR.

where the diffusion coefficient is given by

$$\mathcal{D}(2\omega) = \frac{v_E(2\omega)\ell_t(2\omega)}{3}. \quad (2)$$

For nonresonant scatterers, the energy velocity can be well approximated by $v_E(2\omega) = c/n_r(2\omega)$, where c is the light velocity in vacuum. ℓ_t and ℓ_a are the transport and absorption mean free paths, respectively. a_e and L_e are the effective radius and thickness of the pellet, respectively, and are given by $a_e(2\omega) = a + z_e(2\omega)$ and $L_e(2\omega) = L + 2z_e(2\omega)$, where z_e is the extrapolation length, given by

$$z_e(2\omega) = \frac{2}{3}\ell_t(2\omega) \left[\frac{1 + R(2\omega)}{1 - R(2\omega)} \right]. \quad (3)$$

α_1 in Eq. (1) is the first zero of the zero-order Bessel function J_0 . By fitting the experimentally measured decay rates at $\lambda = 532$ nm for different sample lengths with Eq. (1), we extract $\ell_t(2\omega) \approx 32 \mu\text{m}$ and $\ell_a(2\omega) \approx 11$ mm (side loss). Due to the limitation of spectral sensitivity, the streak camera could not be used for the temporal profile of the IR light and the determination of the transport mean free path. We derived the value of $\ell_t(\omega)$ from a coherent backscattering experiment [40]. The estimated value of $\ell_t(\omega)$ is $\sim 216 \mu\text{m}$. Note that for both the harmonics, $\{L, a\} \gg \ell_t$ and $t \gg v_E \ell_t$. This signifies that our sample is clearly in the diffusive regime [41].

Next, we examine the spatial diffusion profiles in the pellet. Figure 3 displays the experimentally measured spatial profiles for the IG (blue solid line), IR (orange dotted line), and SHG (green dashed line) photons. Each profile shows a characteristic diffusive peak inside the input edge. The first peak to appear is the IG one, followed by the IR one. This behavior is expected since $\ell_t(2\omega) < \ell_t(\omega)$. The SHG peak may be expected to appear at a location where the fundamental intensity is maximum. However, this is not the case, and the maximum intensity of the SHG is observed deeper in the sample where the IR is about 80% of its peak intensity. This

comes from the fact that the SHG beam is generated in the medium by the IR beam and then propagates with the same transport characteristics as the IG beam. This behavior will be well reproduced by the theoretical model. Regarding the wings deep inside the sample, an exponential decay is observed. This arises from the loss mechanisms at play in the sample coming from the finite transverse extent of the pellet, the linear absorption, and the nonlinearity in the case of the IR light.

III. THEORETICAL MODEL

A. Disorder model

In order to give more physical insights, we develop a theoretical model that takes into account multiple scattering and second-harmonic generation. To this end, we generalize the standard multiple-scattering theory to derive transport equations for the fundamental and second-harmonic intensities averaged over the configurations of the disorder. This derivation is similar to that of Ref. [32]. However, there are three major differences: (1) we explicitly consider the time-dependent regime, (2) we drop the intensity decorrelation due to scatterer displacements, and (3) we take absorption into account. It is important to note that this does not change the way the derivation is performed since these differences do not directly enter the computation of the second-harmonic phase function. Interested readers can refer to Appendix B, where the derivation is given. We present in the following only the assumptions and the main results. We first define a model of the disorder. The real material is made of a fine KDP powder containing particles of different shapes and sizes. Therefore, the simplest and most natural disorder model consists of a continuous and complex fluctuating permittivity $\epsilon(\mathbf{r})$. The disorder microstructure is then characterized by a spatial correlation function that is chosen to be Gaussian in the form

$$C_\epsilon(\mathbf{r} - \mathbf{r}', \omega) = \langle \delta\epsilon(\mathbf{r}, \omega) \delta\epsilon^*(\mathbf{r}', \omega) \rangle = |\Delta\epsilon(\omega)|^2 C(\mathbf{r} - \mathbf{r}'), \quad (4)$$

with

$$C(\mathbf{r} - \mathbf{r}') = \exp\left[-\frac{|\mathbf{r} - \mathbf{r}'|^2}{2\ell^2}\right]. \quad (5)$$

In the equations above, $\langle \dots \rangle$ represents an average over all disorder configurations (statistical average). $\delta\epsilon(\mathbf{r}, \omega) = \epsilon(\mathbf{r}, \omega) - \langle \epsilon(\mathbf{r}, \omega) \rangle$ is the fluctuating part of the permittivity, $|\Delta\epsilon(\omega)|^2$ is the amplitude of the correlation, and ℓ is the correlation length. $|\Delta\epsilon(\omega)|^2$ depends on frequency since the permittivity ϵ is dispersive. However, ℓ involves only the geometrical structure of the disorder and thus does not depend on frequency. This also implies that the $\chi^{(2)}$ nonlinearity is supposed to be correlated in a similar way (i.e., with the same correlation length). We thus have

$$\begin{aligned} C_\chi(\mathbf{r} - \mathbf{r}', \omega) &= \langle \chi^{(2)}(\mathbf{r}, \omega) \chi^{(2)*}(\mathbf{r}', \omega) \rangle \\ &= |\Delta\chi(\omega)|^2 C(\mathbf{r} - \mathbf{r}'). \end{aligned} \quad (6)$$

B. Transport equations

We first consider the case of the fundamental beam at frequency ω corresponding to $\lambda = 1064$ nm and also denoted by

IR. The application of the standard multiple-scattering theory leads to the no less standard RTE given by [42]

$$\begin{aligned} &\left[\frac{1}{v_E(\omega)} \frac{\partial}{\partial t} + \mathbf{u} \cdot \nabla_{\mathbf{r}} + \frac{1}{\ell_e(\omega)} \right] I(\mathbf{r}, \mathbf{u}, t, \omega) \\ &= \frac{1}{\ell_s(\omega)} \int p(\mathbf{u}, \mathbf{u}', \omega) I(\mathbf{r}, \mathbf{u}', t, \omega) d\mathbf{u}'. \end{aligned} \quad (7)$$

Although the pellet is large enough, a diffusion-type equation is not adequate enough to describe the experimental results. Indeed, this kind of equation does not allow an accurate reconstruction of the fluxes at short times and/or at small depths. A transport-type equation such as Eq. (7) is required. In this equation, $I(\mathbf{r}, \mathbf{u}, t, \omega)$ is the specific intensity, which can be seen as the radiative flux at position \mathbf{r} , in direction \mathbf{u} , at time t , and at frequency ω . More precisely, the derivation from first principles shows that it is given by the Wigner transform of the field. It reads

$$\begin{aligned} \delta(k - k_r) I(\mathbf{r}, \mathbf{u}, t, \omega) &= \int \left\langle E\left(\mathbf{r} + \frac{\mathbf{s}}{2}, \omega + \frac{\Omega}{2}\right) \right. \\ &\times \left. E^*\left(\mathbf{r} - \frac{\mathbf{s}}{2}, \omega - \frac{\Omega}{2}\right) \right\rangle e^{-i\mathbf{k}\mathbf{u}\cdot\mathbf{s} - i\Omega t} d\mathbf{s} \frac{d\Omega}{2\pi}, \end{aligned} \quad (8)$$

where E is the electric field, with E^* being its complex-conjugate counterpart. In this definition, the electric field is a scalar quantity. Indeed, we choose here to neglect the effect of the polarization, which is a very good approximation in the multiple-scattering regimes where the field can be considered to be fully depolarized [43]. $k_r(\omega) = n_r(\omega)k_0$ is the real part of the effective wave vector, where $k_0 = \omega/c$ is the wave number in vacuum. We recall that n_r is the real part of the effective refractive index. It describes the phase velocity of the average field $\langle E \rangle$ (i.e., the field averaged over all possible configurations of the disorder). $\ell_e(\omega)$ and $\ell_s(\omega)$ are the extinction and scattering mean free paths, respectively. They are connected by the relation $\ell_e(\omega)^{-1} = \ell_s(\omega)^{-1} + \ell_a(\omega)^{-1}$, with $\ell_a(\omega)$ being the absorption mean free path. $p(\mathbf{u}, \mathbf{u}', \omega)$ is the phase function representing the fraction of power scattered from direction \mathbf{u}' to direction \mathbf{u} during a single scattering event. For the Gaussian disorder considered here, it is given by

$$\begin{aligned} p(\mathbf{u}, \mathbf{u}', \omega) &\propto p(|k_r(\omega)\mathbf{u} - k_r(\omega)\mathbf{u}'|), \\ p(q) &= \exp\left[-\frac{q^2\ell^2}{2}\right], \end{aligned} \quad (9)$$

normalized such that $\int p(\mathbf{u}, \mathbf{u}', \omega) d\mathbf{u}' = 1$. As previously mentioned, $v_E(\omega)$ is the energy velocity, well approximated by the phase velocity for nonresonant scatterers. Equation (7) can be easily interpreted using a random-walk picture. In this picture, light undergoes a random walk whose average step is given by the scattering mean free path $\ell_s(\omega)$ and whose angular distribution at each scattering event is given by the phase function $p(\mathbf{u}, \mathbf{u}', \omega)$. The absorption is taken into account along a path of length s through an exponential decay $\exp[-s/\ell_a(\omega)]$.

Let us focus now on the second-harmonic light at frequency 2ω corresponding to $\lambda = 532$ nm and also denoted by

SHG. By generalizing the standard multiple-scattering theory taking into account second-harmonic generation, we obtain a RTE given by (see Appendix B for details)

$$\begin{aligned} & \left[\frac{1}{v_E(2\omega)} \frac{\partial}{\partial t} + \mathbf{u} \cdot \nabla_{\mathbf{r}} + \frac{1}{\ell_e(2\omega)} \right] I(\mathbf{r}, \mathbf{u}, t, 2\omega) \\ &= \frac{1}{\ell_s(2\omega)} \int p(\mathbf{u}, \mathbf{u}', 2\omega) I(\mathbf{r}, \mathbf{u}', t, 2\omega) d\mathbf{u}' \\ &+ \alpha \iint p_{\text{SHG}}(\mathbf{u}, \mathbf{u}', \mathbf{u}'', \omega) I(\mathbf{r}, \mathbf{u}', t, \omega) \\ &\times I(\mathbf{r}, \mathbf{u}'', t, \omega) d\mathbf{u}' d\mathbf{u}'' . \end{aligned} \quad (10)$$

This equation is very similar to Eq. (7), except for the presence of a nonlinear source term. Because of the statistical average over disorder configurations, it can be shown that the dominant contribution in terms of paths for the second-harmonic beam involves two SHG processes (one to generate the field at 2ω and one to generate its complex conjugate) at the same location and time [32]. This implies that there is no phase shift to take into account between two fields, one at frequency ω and one at frequency 2ω , and there is no phase-matching condition as in standard SHG experiments without scattering. Thus, the SHG process reduces to the product of two specific intensities at ω coming from two different directions \mathbf{u}' and \mathbf{u}'' . α is a factor containing all constants involved in the SHG process such as $\chi^{(2)}$. $p_{\text{SHG}}(\mathbf{u}, \mathbf{u}', \mathbf{u}'', \omega)$ is the SHG phase function describing the distribution of the SHG source term in direction \mathbf{u} arising from two linear specific intensities coming from directions \mathbf{u}' and \mathbf{u}'' . In the case of the correlated disorder we consider here, it is given by

$$p_{\text{SHG}}(\mathbf{u}, \mathbf{u}', \mathbf{u}'', \omega) \propto p(|k_r(2\omega)\mathbf{u} - k_r(\omega)\mathbf{u}' - k_r(\omega)\mathbf{u}''|), \quad (11)$$

where the p function is given in Eq. (9) and normalized such that $\int p_{\text{SHG}}(\mathbf{u}, \mathbf{u}', \mathbf{u}'', \omega) d\mathbf{u}' d\mathbf{u}'' = 1$. Thus, the SHG phase function is directly related to the disorder correlation function in the same way as the standard phase function since the SHG and scattering processes both take place in the scatterers. We note that these equations are obtained in the perturbative approach, meaning that the beam at ω is a source term for the beam at 2ω , but the beam at 2ω has a negligible impact on the beam at ω .

C. Numerical simulations

Equations (7) and (10) are solved using a Monte Carlo scheme in geometries as close as possible to that in the real experiments (see Fig. 4 for details). In particular, the crystal grains have sizes ranging from 2 to 8 μm , which is large compared to the wavelength. The correlation length is taken such that $k_0\ell = 3$ for all simulations. Using this value and the experimental estimate of the real part n_r of the effective refractive index, we get estimates for the anisotropy factors of $g(\omega) = 0.95$ and $g(2\omega) = 0.99$. Then the values of the scattering mean free paths are deduced from the experimental estimates of the transport mean free paths using the relation $\ell_s = \ell_t(1 - g)$. Experimental estimates are directly used for the absorption mean free paths ℓ_a . This shows that the disorder correlation length ℓ impacts only ℓ_s . Recalling that ℓ_t are small compared to the dimensions of the pellet, the diffusive

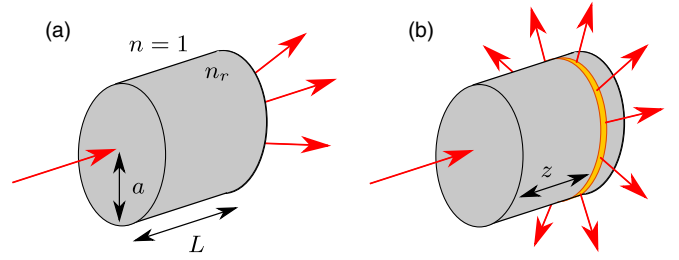


FIG. 4. Geometry considered in the Monte Carlo simulations. The illumination is a Gaussian beam with waist w_i impacting the front face of the pellet under normal incidence. The detection is performed (a) through the back face of the pellet (temporal simulation) or (b) along the side face (spatial simulation). The cylinder contains the powder (pellet) and has a radius a and a height L . The refractive index mismatch between the cylinder (real part of the effective refractive index n_r) and the external medium assumed to be air is also taken into account in the simulation.

regime applies. Thus, ℓ_t is much more important than ℓ_s at large depth and time, and the real value of $k_0\ell$ weakly impacts the numerical results except at small depth and time, where slight variations can occur. In practice, three simulations are performed. The first is done to compute a six-dimensional map (one temporal, three positional, and two directional coordinates) of the specific intensity at ω . It also gives access to the linear detected flux at ω denoted by $F_{\text{IR}}(t)$. The second is done to evaluate the SHG detected flux at 2ω [i.e., $F_{\text{SHG}}(t)$] using the previous map as a source term. The last is performed to estimate the linear detected flux at 2ω [i.e., $F_{\text{IG}}(t)$].

The results are shown in Figs. 5 and 6 for the temporal and spatial profiles, respectively. The specific parameters for each experiment are detailed in the captions and are chosen to mimic the experiments. Both figures show very good agreement with the experiment. Let us first consider the temporal results in Fig. 5. We clearly recover the correct exponential time decay of the flux at long times, which is a feature of the diffusive regime. In particular, the long-time dependence of the flux at the fundamental frequency $F_{\text{IR}}(t)$ is given by $\exp[-\Gamma(\omega)t]$. In the diffusive regime, since all radiative quantities have the same time dependence, the specific intensity itself also decays according to the same law. This implies that the source term of the nonlinear RTE has a long-time dependence given by $\exp[-2\Gamma(\omega)t]$. By convolving this source term with the time response of a short pulse, we simply deduce the long-time behavior of the SHG flux at 2ω , which is given by

$$\begin{aligned} F_{\text{SHG}}(t) &\propto \int_0^t e^{-2\Gamma(\omega)t'} e^{-\Gamma(2\omega)(t-t')} dt' \\ &\propto \begin{cases} \frac{e^{-\Gamma(2\omega)t} - e^{-2\Gamma(\omega)t}}{2\Gamma(\omega) - \Gamma(2\omega)} & \text{if } \Gamma(2\omega) \neq 2\Gamma(\omega), \\ t e^{-\Gamma(2\omega)t} & \text{otherwise.} \end{cases} \end{aligned} \quad (12)$$

For the powder considered here, $2\Gamma(\omega) > \Gamma(2\omega)$, which means that the long-time behavior of the SHG flux is given by $e^{-\Gamma(2\omega)t}$. In other words, the IG and SHG beams have the same time decay at long times. This is clearly seen in Fig. 5. However, we note that a different behavior could have been observed depending on the order relation between $2\Gamma(\omega)$ and $\Gamma(2\omega)$. We also note that Eq. (12) is obtained under the

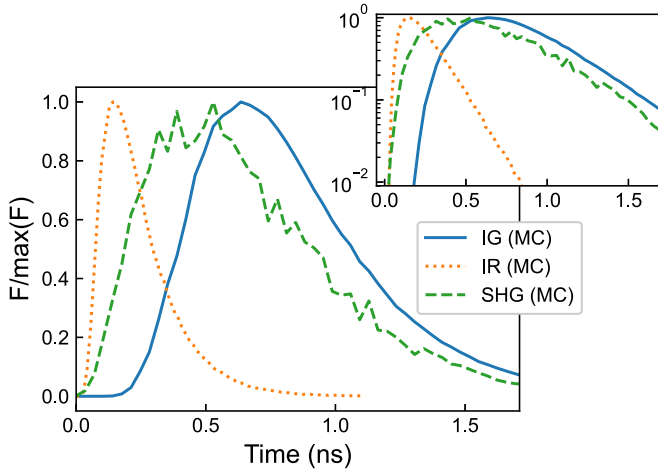


FIG. 5. Numerically simulated temporal transmitted flux profiles of incident green (IG; blue solid line), fundamental infrared (IR; orange dotted line), and second-harmonic-generated green (SHG; green dashed line) light for the $L = 5$ mm pellet. Inset: flux profiles on a semilog scale. We also observe a poorer SNR on the SHG curve. This is due to slow numerical convergence (only a fraction of the SHG light is collected on the detector since the source term for the SHG beam is dispersed throughout the pellet and a large part of the SHG beam emerges from the other sides of the pellet). All parameters are chosen to mimic the experiment. The pellet is illuminated from the front face with an ultrashort Gaussian pulse of normalized waist $k_0 w_i = 2.95 \times 10^4$ (at frequency ω) and $k_0 w_i = 1.77 \times 10^4$ (at frequency 2ω) and under normal incidence. The detection is performed through the back face of the pellet [see Fig. 4(a)]. The other parameters are given by $k_0 a = 2.96 \times 10^4$, $k_0 L = 2.96 \times 10^4$, $k_0 \ell_s(\omega) = 1.28 \times 10^3$, $k_0 \ell_s(2\omega) = 1.89 \times 10^2$, $k_0 \ell_a(\omega) = 1 \times 10^{10}$, $k_0 \ell_a(2\omega) = 5.9 \times 10^5$, $n_r(\omega) = 1.43$, $n_r(2\omega) = 1.45$, and $k_0 \ell = 3$.

assumption of exponential decay at all times for all quantities included in this calculation. Since this is valid only at long times, slight deviations could be observed numerically when comparing the IG and SHG beams. However, Fig. 5 shows that this is not the case. A quick comparison with Fig. 2 reveals very good qualitative agreement with the experiments.

Regarding the spatial distribution of intensity displayed in Fig. 6, we clearly see that the green light in the linear domain shows a maximum right at the input interface of the sample. The fundamental IR light similarly shows a maximum slightly deeper in the sample, obviously owing to the larger value of ℓ_r , which is the consequence of the larger wavelength. The generated second-harmonic light peaks much deeper into the sample, reflecting the process of local generation and subsequent diffusion of the emitted light. These trends accurately reproduce the experimental observations in Fig. 3 in a quantitative manner, certifying the completeness of the numerical model. Overall, for the total spatiotemporal behavior, we can claim the agreement is semiquantitative.

IV. SUMMARY AND CONCLUSIONS

In conclusion, we experimentally and numerically investigated the diffusion of light in a second-order-nonlinear disordered material with a strong nonlinear coefficient. In the experiments, a cylindrical pellet of KDP microcrystals,

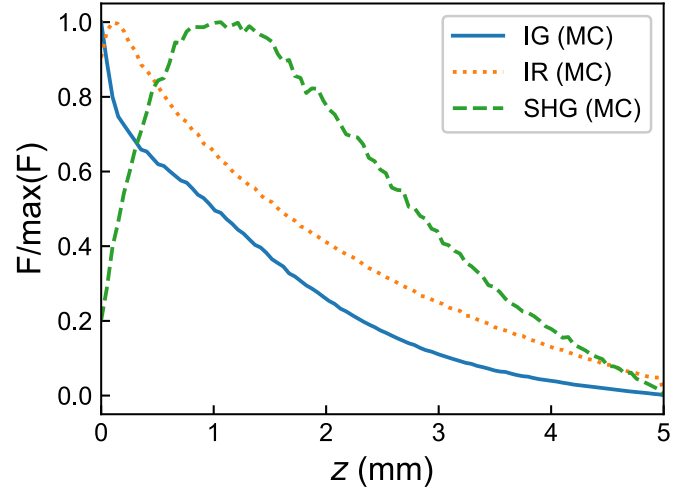


FIG. 6. Numerically simulated spatial flux profiles of incident green (IG; blue solid line), fundamental infrared (IR; orange dotted line), and second-harmonic-generated green (SHG; green dashed line) light for the $L = 5$ mm pellet. Numerical diffusion profiles show excellent agreement with the experimental results in Fig. 3. All parameters are chosen to mimic the experiment. The pellet is illuminated from the front face with a Gaussian beam of normalized waist $k_0 w_i = 2.95 \times 10^4$ (at frequency ω) and $k_0 w_i = 1.77 \times 10^4$ (at frequency 2ω) and under normal incidence. The detection is performed along the side face of the pellet at different depths z [see Fig. 4(b)]. The other parameters are given by $k_0 a = 2.96 \times 10^4$, $k_0 L = 2.96 \times 10^4$, $k_0 \ell_s(\omega) = 1.28 \times 10^3$, $k_0 \ell_s(2\omega) = 1.89 \times 10^2$, $k_0 \ell_a(\omega) = 1 \times 10^{10}$, $k_0 \ell_a(2\omega) = 5.9 \times 10^5$, $n_r(\omega) = 1.43$, $n_r(2\omega) = 1.45$, and $k_0 \ell = 3$.

packed in a random orientation, was employed. The spatial and temporal diffusion profiles of fundamental and second-harmonic light were measured, along with incident light at the second-harmonic wavelength. The experimental data were used to estimate the transport parameters to the best possible accuracy. Next, the experimental results were supported by a theoretical model derived from first principles and led to the coupling of transport equations for the linear and nonlinear beams. A Monte Carlo scheme was used to solve this model numerically in the same geometry as in the experiment. Excellent agreement was obtained for the spatial behavior seen in the experiments, along with very good qualitative agreement for the temporal behavior. Moreover, this model allowed a clear interpretation of the experimental results.

We note that this work addresses spatial and temporal diffusion separately for both fundamental and second-harmonic light. In the domain of linear disorder, researchers have investigated spatiotemporal diffusion [44,45], which has very interesting implications in light transport. Naturally, spatiotemporal diffusion of second-harmonic light simultaneously with the fundamental light will form an exciting frontier in nonlinear disorder physics. Indeed, the streak camera used for this work has the capability to simultaneously capture spatial and temporal diffusion. In addition, in our cylindrical geometry, there is a scope for exploration of transverse diffusion of second-harmonic as well as fundamental light. These topics will form the object of our future studies, starting with the current numerical models. We expect the present work to

lay down the platform for further modeling of light transport in nonlinear disorder.

ACKNOWLEDGMENTS

R.S. and S.M. acknowledge the support from K. K. Iyer and S. K. Upadhyay during the sample making. We also thank B. Chalke for her help with the SEM measurements. R.S. appreciates the support from A. K. Boddeti for the initial experiments. R.S. thanks S. Mondal for fruitful discussions. We express our gratitude to the Department of Atomic Energy, Government of India, for funding for Project Identification No. RTI4002 under DAE OM No. 1303/1/2020/R&D-II/DAE/5567 and for the Swarnajayanti Fellowship, Department of Science and Technology, Ministry of Science and Technology, India. This work also received support under the program “Investissements d’Avenir” launched by the French Government.

The authors declare no conflict of interest.

APPENDIX A: DETERMINATION OF THE EFFECTIVE REFRACTIVE INDICES AND INTERNAL REFLECTION COEFFICIENTS

1. Determination of the real part of the effective refractive index n_r of the random medium

In the pellet, the volume fraction of the KDP is 0.88. The Maxwell-Garnett equation reads [37]

$$\left(\frac{\epsilon_r - \epsilon_m}{\epsilon_r + 2\epsilon_m} \right) = \delta_i \left(\frac{\epsilon_i - \epsilon_m}{\epsilon_i + 2\epsilon_m} \right), \quad (\text{A1})$$

where ϵ_r , ϵ_i , and ϵ_m are the real parts of the dielectric constant of the medium, the inclusions, and the matrix, respectively, and δ_i is the volume fraction of the inclusions. In our case, the air percentage is smaller than the KDP powder. We can therefore assume that air is the inclusion and KDP is the matrix. Setting $\delta_i = 0.12$, $\epsilon_i = 1$, and $\epsilon_m = n_m^2 = (1.5124)^2$, we get $n_r(2\omega) = 1.45$ at $\lambda = 532$ nm. At $\lambda = 1064$ nm, the refractive index of KDP is 1.4938 [46]. The calculated value of $n_r(\omega)$ is 1.4336.

2. Determination of the internal reflection coefficient R

We can obtain an estimate of the reflection coefficient using Fresnel’s law. We assume that the direction and polarization of diffusing light incident on the boundary from inside the sample are completely random and the sample surface is flat. For an angle of incidence θ , the power reflection coefficient $R(\theta)$ averaged over polarization is

$$R(\theta) = \frac{R_{\perp}(\theta) + R_{\parallel}(\theta)}{2}, \quad (\text{A2})$$

where

$$R_{\perp}(\theta) = \left| \frac{n_1 \cos \theta - n_2 \sqrt{1 - \left(\frac{n_1}{n_2} \sin \theta\right)^2}}{n_1 \cos \theta + n_2 \sqrt{1 - \left(\frac{n_1}{n_2} \sin \theta\right)^2}} \right|^2 \quad (\text{A3})$$

and

$$R_{\parallel}(\theta) = \left| \frac{n_1 \sqrt{1 - \left(\frac{n_1}{n_2} \sin \theta\right)^2} - n_2 \cos \theta}{n_1 \sqrt{1 - \left(\frac{n_1}{n_2} \sin \theta\right)^2} + n_2 \cos \theta} \right|^2 \quad (\text{A4})$$

are the Fresnel power reflection coefficients for incident light polarized perpendicular and parallel to the plane of incidence, respectively. Then the power internal reflection coefficient R averaged over the incident angle θ is given by [38]

$$R = \frac{3C_2 + 2C_1}{3C_2 - 2C_1 + 2}, \quad (\text{A5})$$

where

$$C_1 = \int_0^{\frac{\pi}{2}} R(\theta) \sin \theta \cos \theta d\theta \quad (\text{A6})$$

and

$$C_2 = \int_0^{\frac{\pi}{2}} R(\theta) \sin \theta \cos^2 \theta d\theta. \quad (\text{A7})$$

Setting $n_1 = n_r$ and $n_2 = 1$, we get $R(\omega) = 0.52$ (i.e., for $\lambda = 1064$ nm) and $R(2\omega) = 0.53$ (i.e., for $\lambda = 532$ nm).

APPENDIX B: DERIVATIONS OF THE TRANSPORT EQUATIONS

This Appendix is dedicated to the derivations of the transport equations at ω and 2ω . We report here the main steps, and we detail the computation of the SHG source term for the nonlinear transport equation at 2ω . The derivations rely mainly on the standard multiple-scattering theory, the details of which can be found in various books and reviews [2,47–49].

1. Scattering potential and Green’s function

One of the main building blocks of the multiple-scattering theory is the scattering potential defined by

$$V(\mathbf{r}, \omega) = k_0^2 [\epsilon(\mathbf{r}, \omega) - \epsilon_b(\omega)], \quad (\text{B1})$$

where $\epsilon_b(\omega)$ is the permittivity of the background homogeneous medium (reference medium). In order to ensure that the perturbative method applied afterward is as accurate as possible, it is advisable to choose for ϵ_b the statistical average of the permittivity [i.e., $\langle \epsilon(\mathbf{r}, \omega) \rangle$], which leads to

$$V(\mathbf{r}, \omega) = k_0^2 \delta \epsilon(\mathbf{r}, \omega). \quad (\text{B2})$$

This potential describes the scattering process of the heterogeneities of the medium. The second ingredient is the background Green’s function that connects two consecutive scattering events. It is given by

$$G_b(\mathbf{r} - \mathbf{r}', \omega) = \frac{\exp(ik_b |\mathbf{r} - \mathbf{r}'|)}{4\pi |\mathbf{r} - \mathbf{r}'|}, \quad (\text{B3})$$

where $k_b = n_b k_0$ is the wave vector in the background medium. We note that this Green’s function is a scalar quantity here since we choose to neglect the polarization. Indeed, it can be shown that the polarization is completely washed out on average after a propagation distance of the order of the transport mean free path inside a disordered medium [43]. In particular,

this expression given by Eq. (B3) corresponds to the Green's function of the scalar homogeneous wave equation given by

$$\Delta G_b(\mathbf{r} - \mathbf{r}', \omega) + k_b^2 G_b(\mathbf{r} - \mathbf{r}', \omega) = -\delta(\mathbf{r} - \mathbf{r}'). \quad (\text{B4})$$

2. Self-energy and intensity vertex

Two operators are used to describe the propagation of the field in disordered media: the self-energy $\Sigma(\mathbf{r}, \mathbf{r}', \omega)$ entering the Dyson equation that governs the average field propagation and the intensity vertex $\Gamma(\mathbf{r}, \mathbf{r}', \boldsymbol{\rho}, \boldsymbol{\rho}', \omega)$ entering the Bethe-Salpeter equation that governs the field-field correlation evolution. Both contain an infinite series of scattering sequences that are statistically not factorizable. Considering a dilute medium (quantified further by the condition $k_r \ell_e \gg 1$), these scattering sequences can be seen as Taylor expansions. Thus, we can apply a perturbative approach and truncate the series to the first nonzero order. In the following, we consider only the frequency ω , but the same result holds at 2ω (for only the linear beams).

For the self-energy Σ , this gives

$$\Sigma(\mathbf{r}, \mathbf{r}') = \langle V(\mathbf{r}, \omega) G_b(\mathbf{r} - \mathbf{r}', \omega) V(\mathbf{r}', \omega) \rangle_c, \quad (\text{B5})$$

where $\langle \cdot \rangle_c$ represents a statistical average restricted to the connected part, i.e., $\langle V G_b V \rangle_c = \langle V G_b V \rangle - \langle V \rangle G_b \langle V \rangle$. Since the disorder correlation function C depends only on $|\mathbf{r} - \mathbf{r}'|$ (statistical homogeneity and isotropy), we have in the Fourier domain

$$\Sigma(\mathbf{k}, \mathbf{k}', \omega) = 8\pi^3 \delta(\mathbf{k} - \mathbf{k}') \tilde{\Sigma}(k, \omega). \quad (\text{B6})$$

This allows us to define the real part of the effective optical index by

$$n_r(\omega) = n_b + \frac{\text{Re} \tilde{\Sigma}(k_r, \omega)}{2n_r k_0^2}, \quad (\text{B7})$$

where we recall that $k_r(\omega) = n_r(\omega)k_0$ and $k_0 = \omega/c$. This is a closed equation, and the computation of n_r in practice is not an easy task except in very dilute media. That being known, the extinction mean free path is defined by

$$\frac{1}{\ell_e(\omega)} = \frac{\text{Im} \tilde{\Sigma}(k_r, \omega)}{k_r}. \quad (\text{B8})$$

For the intensity vertex Γ , we have

$$\Gamma(\mathbf{r}, \mathbf{r}', \boldsymbol{\rho}, \boldsymbol{\rho}', \omega) = \langle V(\mathbf{r}, \omega) V^*(\boldsymbol{\rho}, \omega) \rangle_c \delta(\mathbf{r}' - \mathbf{r}') \delta(\boldsymbol{\rho} - \boldsymbol{\rho}'). \quad (\text{B9})$$

By invoking once again the statistical homogeneity and isotropy, we get into the Fourier domain

$$\Gamma(\mathbf{k}, \mathbf{k}', \boldsymbol{\kappa}, \boldsymbol{\kappa}', \omega) = 8\pi^3 \delta(\mathbf{k} - \mathbf{k}' - \boldsymbol{\kappa} + \boldsymbol{\kappa}') \tilde{\Gamma}(\mathbf{k}, \mathbf{k}', \boldsymbol{\kappa}, \boldsymbol{\kappa}', \omega), \quad (\text{B10})$$

which leads to the following expressions for the phase function and the scattering mean free path:

$$\frac{1}{\ell_s(\omega)} p(\mathbf{u}, \mathbf{u}', \omega) = \frac{1}{16\pi^2} \tilde{\Gamma}(k_r \mathbf{u}, k_r \mathbf{u}', k_r \mathbf{u}, k_r \mathbf{u}', \omega), \quad (\text{B11})$$

with the normalization

$$\int p(\mathbf{u}, \mathbf{u}', \omega) d\mathbf{u}' = 1. \quad (\text{B12})$$

This finally leads to

$$\frac{1}{\ell_s(\omega)} = \frac{k_0^2 |\Delta\epsilon|^2}{16\pi^2} \int_{4\pi} C(\mathbf{q}) d\mathbf{u}', \quad (\text{B13})$$

$$p(\mathbf{u}, \mathbf{u}', \omega) = C(\mathbf{q}) \left[\int_{4\pi} C(\mathbf{q}) d\mathbf{u}' \right]^{-1} \quad (\text{B14})$$

$$= \frac{k_r^2 \ell^2 \exp[-q^2 \ell^2 / 2]}{2\pi [1 - \exp(-2k_r^2 \ell^2)]}, \quad (\text{B15})$$

with $\mathbf{q} = k_r(\mathbf{u} - \mathbf{u}')$ and $C(\mathbf{q})$ being the Fourier transform of the disorder correlation function C . In the case of a nonabsorbing medium where the imaginary part of the permittivity vanishes, we have, from Eqs. (B8) and (B13),

$$\frac{1}{\ell_e(\omega)} = \frac{1}{\ell_s(\omega)} = \frac{k_0^2 |\Delta\epsilon|^2}{16\pi^2} \int_{4\pi} C(k_r(\mathbf{u} - \mathbf{u}')) d\mathbf{u}', \quad (\text{B16})$$

which implies that $\ell_e^{-1}(\omega) = 0$. In practice for the numerical simulations performed in this study, the parameters n_r , ℓ_e , and ℓ_s are not computed using Σ and Γ and are given by experimental measurements. However, Eq. (B15) is used for the profile of the phase function.

3. Transport equation in the linear regime

Let us first consider the transport equation at ω in the linear regime. Considering a dilute medium such that $k_r \ell_e(\omega) \gg 1$, we can show that the dominant term in the field-field correlation function is given by the well-known ladder diagram:

$$\begin{array}{c} E(\mathbf{r}, \omega) \text{ --- } \bigcirc \text{ --- } \bigcirc \text{ --- } \bigcirc \text{ --- } \text{---} E_0 \\ | \quad | \quad | \\ E^*(\mathbf{r}, \omega) \text{ --- } \bigcirc \text{ --- } \bigcirc \text{ --- } \bigcirc \text{ --- } \text{---} E_0^* \end{array} \quad (\text{B17})$$

In this representation, the top line represents a path for the electric field E , and the bottom line is for a path of its complex conjugate E^* . Solid and dashed thick lines correspond to average Green's functions (describing propagation between consecutive scattering events) and average fields, respectively. Circles denote scattering events, and vertical dashed lines represent statistical correlations between scattering events through Eq. (B9). This diagram shows that the field-field correlation function evolution essentially reduces to the propagation of intensity. This implies that the field-field correlation function is governed by a transport equation, namely, the radiative-transfer equation (RTE), which reads

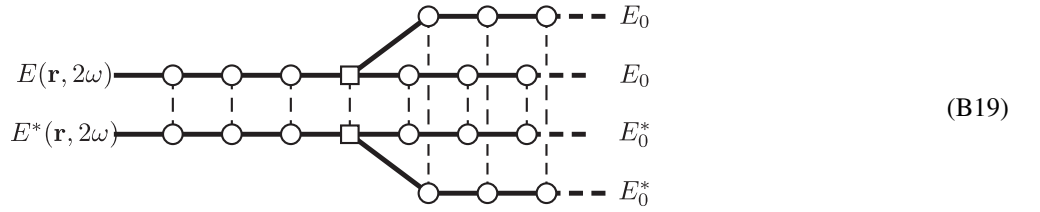
$$\begin{aligned} & \left[\frac{1}{v_E(\omega)} \frac{\partial}{\partial t} + \mathbf{u} \cdot \nabla_r + \frac{1}{\ell_e(\omega)} \right] I(\mathbf{r}, \mathbf{u}, t, \omega) \\ & = \frac{1}{\ell_s(\omega)} \int p(\mathbf{u}, \mathbf{u}', \omega) I(\mathbf{r}, \mathbf{u}', t, \omega) d\mathbf{u}', \end{aligned} \quad (\text{B18})$$

which is Eq. (7).

4. Transport equation in the second-harmonic regime

Since we consider a perturbative approach for the SHG, the main point to address in that case is the expression of the source term. We can show theoretically and validate

numerically [32] that the leading diagram is given by



where the squares denote the second-harmonic processes. This diagram confirms that a transport equation for the SHG beam is still valid, but with a source term given by the product of two specific intensities at ω . In terms of an equation, this source term is given by

$$S(\mathbf{r}, \boldsymbol{\rho}, 2\omega) = \int \langle G(\mathbf{r} - \mathbf{r}', 2\omega) \rangle \langle G^*(\boldsymbol{\rho} - \boldsymbol{\rho}', 2\omega) \rangle \Gamma_{\text{SHG}}(\mathbf{r}', \mathbf{r}'', \mathbf{r}''', \boldsymbol{\rho}', \boldsymbol{\rho}'', \boldsymbol{\rho}''', \omega) \\ \times \langle E(\mathbf{r}'', \omega) E^*(\boldsymbol{\rho}'', \omega) \rangle \langle E(\mathbf{r}''', \omega) E^*(\boldsymbol{\rho}''', \omega) \rangle d\mathbf{r}' d\mathbf{r}'' d\mathbf{r}''' d\boldsymbol{\rho}' d\boldsymbol{\rho}'' d\boldsymbol{\rho}''', \quad (\text{B20})$$

where Γ_{SHG} is the SHG vertex, given by

$$\Gamma_{\text{SHG}}(\mathbf{r}, \mathbf{r}', \mathbf{r}'', \boldsymbol{\rho}, \boldsymbol{\rho}', \boldsymbol{\rho}'', \omega) = \langle \chi^{(2)}(\mathbf{r}, \omega) \chi^{(2)*}(\boldsymbol{\rho}, \omega) \rangle_c \delta(\mathbf{r} - \mathbf{r}') \delta(\mathbf{r} - \mathbf{r}'') \delta(\boldsymbol{\rho} - \boldsymbol{\rho}') \delta(\boldsymbol{\rho} - \boldsymbol{\rho}''). \quad (\text{B21})$$

In the last expression, we keep the complex-conjugate notation for the second-order susceptibility $\chi^{(2)}$ even though it is a real quantity in order to remember that it corresponds to the complex-conjugate field. In the Fourier domain, making use of the statistical homogeneity and isotropy again, we get

$$\widetilde{\Gamma}_{\text{SHG}}(\mathbf{k}, \mathbf{k}', \mathbf{k}'', \boldsymbol{\kappa}, \boldsymbol{\kappa}', \boldsymbol{\kappa}'', \omega) = 8\pi^3 \delta(\mathbf{k} - \mathbf{k}' - \mathbf{k}'' - \boldsymbol{\kappa} + \boldsymbol{\kappa}' + \boldsymbol{\kappa}'') \Gamma_{\text{SHG}}(\mathbf{k}, \mathbf{k}', \mathbf{k}'', \boldsymbol{\kappa}, \boldsymbol{\kappa}', \boldsymbol{\kappa}'', \omega). \quad (\text{B22})$$

From this, we can define a SHG phase function,

$$\alpha p_{\text{SHG}}(\mathbf{u}, \mathbf{u}', \mathbf{u}'', \omega) = \frac{1}{125\pi^5} \widetilde{\Gamma}_{\text{SHG}}(k_r(2\omega)\mathbf{u}, k_r(\omega)\mathbf{u}', k_r(\omega)\mathbf{u}'', k_r(2\omega)\mathbf{u}, k_r(\omega)\mathbf{u}', k_r(\omega)\mathbf{u}'', \omega). \quad (\text{B23})$$

α is a coefficient that takes into account all constants involved in the second-harmonic generation and is such that the second-harmonic phase function is normalized as

$$\int p_{\text{SHG}}(\mathbf{u}, \mathbf{u}', \mathbf{u}'', \omega) d\mathbf{u}' d\mathbf{u}'' = 1. \quad (\text{B24})$$

Plugging in the expression for the correlation function C_χ leads to

$$p_{\text{SHG}}(\mathbf{u}, \mathbf{u}', \mathbf{u}'', \omega) \propto \exp\left[-\frac{q^2 \ell^2}{2}\right], \quad (\text{B25})$$

where $\mathbf{q} = k_r(2\omega)\mathbf{u} - k_r(\omega)\mathbf{u}' - k_r(\omega)\mathbf{u}''$ is the SHG scattering vector. We finally end up with the nonlinear RTE given by

$$\left[\frac{1}{v_E(2\omega)} \frac{\partial}{\partial t} + \mathbf{u} \cdot \nabla_{\mathbf{r}} + \frac{1}{\ell_e(2\omega)} \right] I(\mathbf{r}, \mathbf{u}, t, 2\omega) = \frac{1}{\ell_s(2\omega)} \int p(\mathbf{u} \cdot \mathbf{u}', 2\omega) I(\mathbf{r}, \mathbf{u}', t, 2\omega) d\mathbf{u}' \\ + \alpha \iint p_{\text{SHG}}(\mathbf{u}, \mathbf{u}', \mathbf{u}'', \omega) I(\mathbf{r}, \mathbf{u}', t, \omega) I(\mathbf{r}, \mathbf{u}'', t, \omega) d\mathbf{u}' d\mathbf{u}'', \quad (\text{B26})$$

which is Eq. (10).

-
- [1] A. Ishimaru, *Wave Propagation and Scattering in Random Media* (Academic Press, New York, 1978).
[2] R. Carminati and J. Schotland, *Principles of Scattering and Transport of Light* (Cambridge University Press, Cambridge, 2021).
[3] F. Martelli, S. D. Bianco, A. Ismaelli, and G. Zaccanti, *Light Propagation through Biological Tissue and Other Diffusive Media: Theory, Solutions, and Software* (SPIE Press, Bellingham, WA, 2009).

- [4] C. Kittel, *Introduction to Solid State Physics* (Wiley, Hoboken, NJ, 2012).
[5] V. V. Tuchin, *Tissue Optics: Light Scattering Methods and Instruments for Medical Diagnosis* (SPIE, Bellingham, WA, 2007).
[6] P. W. Anderson, Absence of diffusion in certain random lattices, *Phys. Rev.* **109**, 1492 (1958).
[7] V. S. Letokhov, Generation of light by a scattering medium with negative resonance absorption, *Sov. Phys. JETP* **26**, 835 (1968).

- [8] N. M. Lawandy, R. M. Balachandran, A. S. L. Gomes, and E. Sauvain, Laser action in strongly scattering media, *Nature (London)* **368**, 436 (1994).
- [9] P. Pradhan and N. Kumar, Localization of light in coherently amplifying random media, *Phys. Rev. B* **50**, 9644(R) (1994).
- [10] D. S. Wiersma, The physics and applications of random lasers, *Nat. Phys.* **4**, 359 (2008).
- [11] A. K. Tiwari and S. Mujumdar, Random lasing over gap states from a quasi-one-dimensional amplifying periodic-on-average random superlattice, *Phys. Rev. Lett.* **111**, 233903 (2013).
- [12] R. Uppu and S. Mujumdar, Exponentially tempered Lévy sums in random lasers, *Phys. Rev. Lett.* **114**, 183903 (2015).
- [13] V. A. Melnikov, L. A. Golovan, S. O. Konorov, D. A. Muzychenko, A. B. Fedotov, A. M. Zheltikov, V. Y. Timoshenko, and P. K. Kashkarov, Second-harmonic generation in strongly scattering porous gallium phosphide, *Appl. Phys. B* **79**, 225 (2004).
- [14] J. F. de Boer, A. Lagendijk, R. Sprik, and S. Feng, Transmission and reflection correlations of second harmonic waves in nonlinear random media, *Phys. Rev. Lett.* **71**, 3947 (1993).
- [15] Y. Qiao, F. Ye, Y. Zheng, and X. Chen, Cavity-enhanced second-harmonic generation in strongly scattering nonlinear media, *Phys. Rev. A* **99**, 043844 (2019).
- [16] J. Fröhlich, T. Spencer, and C. E. Wayne, Localization in disordered, nonlinear dynamical systems, *J. Stat. Phys.* **42**, 247 (1986).
- [17] M. J. McKenna, R. L. Stanley, and J. D. Maynard, Effects of nonlinearity on Anderson localization, *Phys. Rev. Lett.* **69**, 1807 (1992).
- [18] T. Schwartz, G. Bartal, S. Fishman, and M. Segev, Transport and Anderson localization in disordered two-dimensional photonic lattices, *Nature (London)* **446**, 52 (2007).
- [19] S. Fishman, Y. Krivolapov, and A. Soffer, The nonlinear Schrödinger equation with a random potential: Results and puzzles, *Nonlinearity* **25**, R53 (2012).
- [20] Y. Lahini, A. Avidan, F. Pozzi, M. Sorel, R. Morandotti, D. N. Christodoulides, and Y. Silberberg, Anderson localization and nonlinearity in one-dimensional disordered photonic lattices, *Phys. Rev. Lett.* **100**, 013906 (2008).
- [21] A. Heiderich, R. Maynard, and B. A. van Tiggelen, Coherent backscattering in nonlinear media, *Opt. Commun.* **115**, 392 (1995).
- [22] T. Wellens, B. Grémaud, D. Delande, and C. Miniatura, Coherent backscattering of light by nonlinear scatterers, *Phys. Rev. E* **71**, 055603(R) (2005).
- [23] V. M. Agranovich and V. E. Kravtsov, Effects of weak localization of photons in nonlinear optics: Second harmonic generation, *Phys. Lett. A* **131**, 378 (1988).
- [24] K. M. Yoo, S. Lee, Y. Takiguchi, and R. R. Alfano, Search for the effect of weak photon localization in second-harmonic waves generated in a disordered anisotropic nonlinear medium, *Opt. Lett.* **14**, 800 (1989).
- [25] H. J. Simon, Y. Wang, L.-B. Zhou, and Z. Chen, Coherent backscattering of optical second-harmonic generation with long-range surface plasmons, *Opt. Lett.* **17**, 1268 (1992).
- [26] Y. Wang and H. J. Simon, Coherent backscattering of optical second-harmonic generation in silver films, *Phys. Rev. B* **47**, 13695 (1993).
- [27] P. A. Franken, A. E. Hill, C. W. Peters, and G. Weinreich, Generation of optical harmonics, *Phys. Rev. Lett.* **7**, 118 (1961).
- [28] R. Savo, A. Morandi, J. S. Müller, F. Kaufmann, F. Timpu, M. R. Escalé, M. Zanini, L. Isa, and R. Grange, Broadband Mie driven random quasi-phase-matching, *Nat. Photon.* **14**, 740 (2020).
- [29] J. S. Müller, A. Morandi, R. Grange, and R. Savo, Modeling of random quasi-phase-matching in birefringent disordered media, *Phys. Rev. Appl.* **15**, 064070 (2021).
- [30] A. Morandi, R. Savo, J. S. Müller, S. Reichen, and R. Grange, Multiple scattering and random quasi-phase-matching in disordered assemblies of LiNbO₃ nanocubes, *ACS Photon.* **9**, 1882 (2022).
- [31] R. Samanta and S. Mujumdar, Intensity-dependent speckle contrast of second harmonic light in a nonlinear disordered medium, *Appl. Opt.* **59**, 11266 (2020).
- [32] R. Samanta, R. Pierrat, R. Carminati, and S. Mujumdar, Speckle decorrelation in fundamental and second-harmonic light scattered from nonlinear disorder, *Phys. Rev. Appl.* **18**, 054047 (2022).
- [33] V. E. Kravtsov, V. M. Agranovich, and K. I. Grigorishin, Theory of second-harmonic generation in strongly scattering media, *Phys. Rev. B* **44**, 4931 (1991).
- [34] E. V. Makeev and S. E. Skipetrov, Second harmonic generation in suspensions of spherical particles, *Opt. Commun.* **224**, 139 (2003).
- [35] S. Faez, P. M. Johnson, D. A. Mazurenko, and A. Lagendijk, Experimental observation of second-harmonic generation and diffusion inside random media, *J. Opt. Soc. Am. B* **26**, 235 (2009).
- [36] K. Itoh, T. Matsubayashi, E. Nakamura, and H. Motegi, X-ray study of high-temperature phase transitions in KH₂PO₄, *J. Phys. Soc. Jpn.* **39**, 843 (1975).
- [37] T. C. Choy, *Effective Medium Theory* (Clarendon, Oxford, 1999).
- [38] J. X. Zhu, D. J. Pine, and D. A. Weitz, Internal reflection of diffusive light in random media, *Phys. Rev. A* **44**, 3948 (1991).
- [39] P. Gaikwad, S. Ungureanu, R. Backov, K. Vynck, and R. A. L. Vallée, Photon transport in cylindrically-shaped disordered meso-macroporous materials, *Opt. Express* **22**, 7503 (2014).
- [40] G. Maret and P. E. Wolf, Multiple light scattering from disordered media: The effect of Brownian motion of scatterers, *Z. Phys. B* **65**, 409 (1987).
- [41] Z. Q. Zhang, I. P. Jones, H. P. Schriemer, J. H. Page, D. A. Weitz, and P. Sheng, Wave transport in random media: The ballistic to diffusive transition, *Phys. Rev. E* **60**, 4843 (1999).
- [42] S. Chandrasekhar, *Radiative Transfer* (Dover, New York, 1950).
- [43] K. Vynck, R. Pierrat, and R. Carminati, Polarization and spatial coherence of electromagnetic waves in uncorrelated disordered media, *Phys. Rev. A* **89**, 013842 (2014).
- [44] L. Pattelli, R. Savo, M. Burrelli, and D. S. Wiersma, Spatio-temporal visualization of light transport in complex photonic structures, *Light: Sci. Appl.* **5**, e16090 (2016).
- [45] T. Sperling, L. Schertel, M. Ackermann, G. J. Aubry, C. M. Aegerter, and G. Maret, Can 3D light localization be reached in ‘white paint’? *New J. Phys.* **18**, 013039 (2016).

- [46] KDP refractive index dataset, <https://refractiveindex.info/?shelf=main&book=KH2PO4&page=Zernike-o>.
- [47] S. M. Rytov, Y. A. Kravtsov, and V. I. Tatarskii, *Principles of Statistical Radiophysics* (Springer, Berlin, 1989), Vol. 4.
- [48] L. A. Apresyan and Y. A. Kravtsov, *Radiation Transfer: Statistical and Wave Aspects* (Gordon and Breach, Amsterdam, 1996).
- [49] M. C. W. van Rossum and T. M. Nieuwenhuizen, Multiple scattering of classical waves: Microscopy, mesoscopy and diffusion, *Rev. Mod. Phys.* **71**, 313 (1999).